Surface Pressure Tide Climatologies Deduced from a Quality-Controlled Network of Barometric Observations*

MICHAEL SCHINDELEGGER

Department of Geodesy and Geoinformation, Vienna University of Technology, Vienna, Austria

RICHARD D. RAY

NASA Goddard Space Flight Center, Greenbelt, Maryland

(Manuscript received 1 July 2014, in final form 14 August 2014)

ABSTRACT

Global "ground truth" knowledge of solar diurnal S_1 and semidiurnal S_2 surface pressure tides as furnished by barometric in situ observations represents a valuable standard for wide-ranging geophysical and meteorological applications. This study attempts to aid validations of the air pressure tide signature in current climate or atmospheric analysis models by developing a new global assembly of nearly 6900 mean annual S_1 and S_2 estimates on the basis of station and marine barometric reports from the International Surface Pressure Databank, version 2 (ISPDv2), for a principal time span of 1990–2010. Previously published tidal compilations have been limited by inadequate spatial coverage or by internal inconsistencies and outliers from suspect tidal analyses; here, these problems are mostly overcome through 1) automated data filtering under ISPDv2's quality-control framework and 2) a meticulously conducted visual inspection of station harmonic decompositions. The quality of the resulting compilation is sufficient to support global interpolation onto a reasonably fine mesh of 1° horizontal spacing. A multiquadric interpolation algorithm, with parameters fine-tuned by frequency and for land or ocean regions, is employed. Global charts of the gridded surface pressure climatologies are presented, and these are mapped to a wavenumber versus latitude spectrum for comparison with long-term means of S_1 and S_2 from four present-day atmospheric analysis systems. This cross verification, shown to be feasible even for the minor stationary modes of the tides, reveals a small but probably significant overestimation of up to 18% for peak semidiurnal amplitudes as predicted by global analysis models.

1. Introduction

One of the most pronounced features of Earth's climate and weather are global-scale solar tides in the atmosphere persisting at frequencies that evenly divide into a mean 24-h day. Observational and theoretical considerations have provided a largely detailed picture of these oscillations with predominantly diurnal (24 h, shorthand notation S_1) and semidiurnal (12 h, S_2) periodicity (Chapman and Lindzen 1970; Forbes and Garrett 1979; Hsu and Hoskins 1989; Dai and Wang 1999, hereafter DW; Hagan and Forbes 2002, 2003; Dai and Trenberth 2004; Zhang et al. 2006, and references therein). Their decomposition from a global domain to Fourier space produces a harmonic spectrum dominated by sun-synchronous, westward-propagating waves of uniform local time appearance across all longitudes. The thermal forcing of these "migrating" oscillations by cyclic absorption processes in the middle and lower atmosphere is now well understood [see, e.g., Hagan et al. (2003) for a concise overview]. To first order, solar heating of the ozone layer by ultraviolet radiation excites the main sun-synchronous S_2 tide, which is capable of efficient vertical propagation owing to wavelengths greater than 300 km. By contrast, most of the diurnal harmonics associated with stratospheric heating goes into a vertically trapped mode (Chapman and Lindzen 1970; Covey et al. 2011),

Denotes Open Access content.

* Supplemental information related to this paper is available at the Journals Online website: http://dx.doi.org/10.1175/MWR-D-14-00217.s1.

Corresponding author address: Michael Schindelegger, Department of Geodesy and Geoinformation, Vienna University of Technology, Gußhausstraße 27-29, A-1040 Vienna, Austria.
E-mail: michael.schindelegger@tuwien.ac.at

DOI: 10.1175/MWR-D-14-00217.1

leaving the migrating component of S_1 much more the result of infrared absorption by tropospheric water vapor. The regional variability of this excitation combined with destructive interference of short vertical wavelengths (<30 km) acts to attenuate the signature of S_1 in surface atmospheric parameters despite the obvious diurnal periodicity of incoming solar radiation. ''Nonmigrating'' waves, which are not locked to the apparent motion of the sun, are caused by zonal modulations in the local time behavior of the daily heating cycle. Major contributions to this asymmetric tidal forcing emanate from latent heat released in the wake of deep tropical convective activity (Hagan and Forbes 2002, 2003) and upward sensible heat flux from the ground (Tsuda and Kato 1989). Semidiurnal surface tides in particular are subject to a local-/regional-scale modulation across steep topography (Hamilton et al. 2008), and mass imbalances between evaporation and precipitation over adjacent land and water surfaces might induce additional diurnal atmospheric oscillations (DW).

While a bulk of recent studies has dealt with the significant day-to-day features in the dynamics of the upper atmosphere, most of the pre-satellite-era research concerning solar tides has been confined to theoretical descriptions or to analyses of meteorological surface parameters, particularly of variations in the air pressure p. The local barometer exhibits strong semidiurnal oscillations $S_2 = S_2(p)$, peaking usually 2–3 h before noon (and midnight) with amplitudes that exceed 120 Pa in the tropics but decrease toward the poles. The well-known uniformity of S_2 with respect to longitude highlights the influence of the migrating response to ozone heating, whereas the solar diurnal surface pressure tide $S_1 = S_1(p)$ has more obvious geographical modulations because of the presence of prominent nonmigrating modes over continents. Local wind and temperature variation may accentuate S_1 beyond 180 Pa, which contrasts with the rather small (<70 Pa) migrating component that accounts for the main diurnal pressure signals over the open oceans at a phase lead of 6–7 h with respect to the mean sun.

Reliable knowledge of the global-/regional-scale characteristics of S_1 and S_2 gradually evolved in the twentieth century on the basis of single-station observational determinations throughout the world. Multiyear time series of hourly (or somewhat coarser sampled) barometric measurements, often collected and carefully examined for tidal oscillations by individual researchers, were subject to global analyses first by Simpson (1918) and later by Haurwitz (1956), both addressing the annual mean component of S_2. Haurwitz and Cowley (1973) computed annual and seasonal spherical harmonic expansions of S_1 and S_2 after subjective interpolation of 264 station tide estimates onto a 10° × 15° latitude–longitude grid. Subsequent extensions of this network (Hamilton 1980b; Ray 1998), compiled to a total of 428 stations by Ray (2001), partly redressed data gaps over the open oceans, the Southern Hemisphere, and polar regions, and this merger is still likely to represent the most accurate ''ground truth'' sample of barometric tides. In terms of comprehensiveness, it has, however, been superseded by the dataset of DW, which was built upon surface pressure recordings at 7553 land stations from archives of raw synoptic weather reports along with 3083 marine estimates from the Comprehensive Ocean–Atmosphere Data Set (COADS). The spatial sampling of the DW tidal data is near perfect, but such an extensive compilation necessarily requires automated processing, whereby it becomes difficult to avoid outliers that impact the internal consistency of the dataset (e.g., Ray 2001); see also sections 2 and 4 below. To bridge the obvious gap between such a comprehensive but arguably subpar assembly of in situ tidal estimates and the more limited but evidently higher-quality data of Haurwitz and Cowley (1973) and Ray (2001) is a primary goal of the present study.

Over the last two to three decades, increasingly credible definitions of surface pressure tides have been established with the aid of numerical models of the general atmospheric circulation. Early estimates from free-running forward integrations with rather low wavenumber truncation (Zwiers and Hamilton 1986) are now superseded by simulations at very fine resolution that facilitate the study of local terrain effects on S_1 and S_2 (Hamilton et al. 2008). Such circulation models are also routinely tied to real observational constraints from meteorological measurements within assimilation analyses of the world's main weather agencies. Tidal oscillations in the surface pressure products from these centers have been studied both in their own right (Hsu and Hoskins 1989; van den Dool et al. 1997; Ray and Ponte 2003) and in the context of geophysical applications such as Earth's geometrical and rotational field (Petrov and Boy 2004; Yseboodt et al. 2002). Parts of this scientific ''vogue'' clearly reside in the availability of global pressure fields at uniform spatiotemporal resolution as well as their ''optimal'' nature that accounts for consistency between the laws of physics and the observations given their range of uncertainty.

To some extent, the skill of present-day numerical circulation models poses the question of whether it is still worthwhile to conduct a global analysis of station tide estimates. A range of potential applications (see section 2) supports such an endeavor, though, and there are several conceptual arguments suggesting that estimates from global numerical models do not necessarily mirror the true tides.

1) Conventional atmospheric analysis systems—primarily designed for medium-range weather forecasting or assessing climate conditions in the past and the future—account for tidal oscillations in a rather en passant manner, without complying to the possibly optimal model configuration to reproduce atmospheric dynamics on daily or shorter time scales. Physical parameterizations (for land–sea–air fluxes, turbulence, moist convection, etc.) that have been shown to aid the description of lower-frequency atmospheric circulations lead to inadequacies in the representation of solar tides and the diurnal cycle in particular (Dai and Trenberth 2004; Sato et al. 2008). For example, well-known model deficiencies in terms of convective precipitation (Bechtold et al. 2004) might ultimately feed back to the large uncertainties (>50 Pa) of nonmigrating diurnal pressure oscillations over tropical landmasses, as documented in Schindelegger (2014). Model discretizations and vertical domains may be revisited in a similar manner, taking into account that rigid-lid boundaries likely create spurious resonances of S_2 at the surface (Hamilton et al. 2008).
2) Assimilated samples of barometer recordings in each analysis cycle depart from an optimal spatiotemporal coverage, allowing the model physics or observations from other and probably less suited (non in situ) sensors to affect the signature of surface pressure tides in the output data.
3) With the exception of forecasts issued at short time intervals, the typical sampling of the higher-quality analysis fields still remains 6 h. This causes S_2 to alias into a standing wave and S_1 to be somewhat distorted by folding of the small terdiurnal pressure tide (Ray and Poulose 2005).

As already implied, the purpose of this paper is to advance previously published global analyses of station barometric tides (DW; Ray 2001) by striking a balance between both the necessity of individually valid and reliable tidal estimates and the quest for an optimal spatial coverage over land and oceans. The backbone of this effort is an extensive assembly of multiyear subsets from the recently compiled International Surface Pressure Databank, version 2 (ISPDv2; Compo et al. 2010), which constitutes the world's largest collection of surface pressure and sea level pressure (SLP) observations for the time span 1768–2010. An early precursor of these data archives was in fact used by DW in the form of raw pressure reports from the Global Telecommunication System (GTS). However, the ISPDv2 sets itself apart from such loose assemblies of observations by being embedded in the rigorous quality-control procedure of the Twentieth Century Reanalysis, version 2 (20CRv2), which has been conceived as a consistent twentieth-century reanalysis on the sole basis of surface pressure reports (Compo et al. 2011). This setting facilitates the approximate elimination of defective pressure observations by automated means, and in combination with a visual inspection of the fitted tides at each station, it can largely guarantee that the final S_1/S_2 estimates are both comprehensive and accurate.

The second major undertaking of the present study is to deduce globally gridded climatologies of both principal barometric tides by aid of objective interpolation with the now widely cited multiquadric technique of Nuss and Titley (1994). We devote attention to the choice of the multiquadric parameter and the amount of smoothing, both quantities being of considerable importance for the behavior of S_1 and S_2 in nonuniformly sampled and data-void regions. The chosen horizontal spacing of 1° in latitude and longitude is unprecedented, resulting in a well-resolved wavenumber decomposition that can be juxtaposed to those of global numerical analyses. We investigate the feasibility of such a cross verification for the main migrating and the stationary (zero wavenumber) components of both S_1 and S_2. Our efforts are limited to the annual mean of the surface pressure tides, while locally strong seasonal modulations (20–30 Pa for S_1 over certain landmasses in midlatitudes) await separate treatment in a future publication.

The paper is organized as follows. Section 2 discusses the merits of the DW dataset but also points out inadequacies that a new station tide analysis can improve upon. Supplemental S_1 and S_2 solutions from global analysis models are introduced in section 3, followed by a description of how tidal estimates were retrieved from land and marine in situ barometric measurements (section 4). Intermediate quality assessments of the surface tide data lay the groundwork for gridding by multiquadric interpolation in section 5. Having selected a plausible set of shape parameters for the interpolating functions, we finally examine the new empirical model in terms of its global structure and some selected wavenumber components in section 6.

2. Brief review of the DW station tide data and their empirical model

DW derived mean annual harmonics of S_1 and S_2 and their seasonal variability for a total of 10 620 land stations and ocean boxes from the pressure data of weather stations, commercial ships, and ocean buoys as archived by GTS and COADS during 1976–97 (2 years less for the case of marine reports). In situ estimates from only those stations with more than 4 years of data were retained at

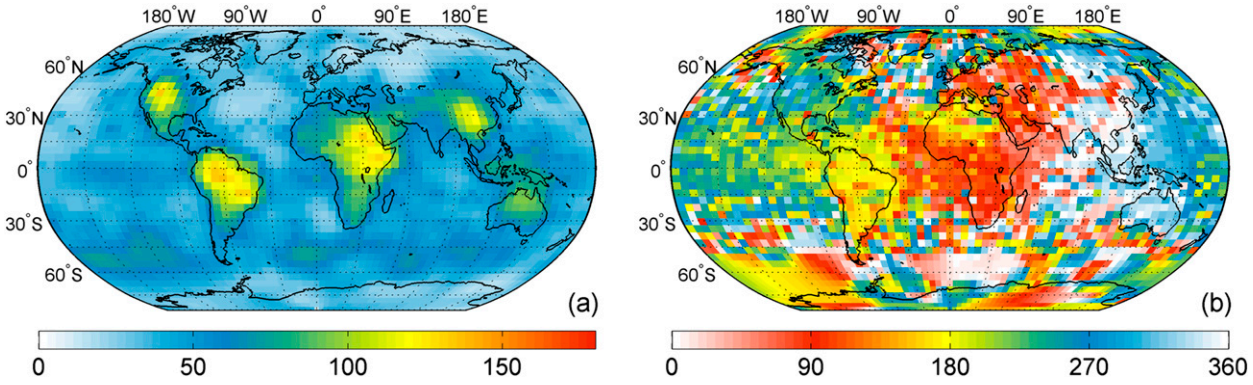

FIG. 1. (a) Annual mean of the diurnal surface pressure amplitudes (Pa) and (b) the corresponding phase lags (°) relative to 0000 UTC as determined by DW on a 4° × 5° latitude–longitude grid.

a preferred temporal sampling of 3 h, though frequent data gaps and the use of some 6-hourly reports in the southern oceans could not be avoided. The recovered network had dense clusters in Europe, the eastern United States, and Southeast Asia and was understandably sparse in polar and subpolar regions and also in central Africa (Fig. 1 of DW).

Extended to a globally gridded domain at 4° × 5° latitude–longitude spacing, the DW model yielded insight into the regional-/continental-scale features of barometric tides and allowed for an illustration of how closely differential sensible heating relates to the S_1 behavior over land and water surfaces. Applications of the DW dataset are varied and include validations of the pressure tide signature in coupled global climate models (Covey et al. 2011, 2014), determinations of the subdaily wind variability over the tropical Pacific (Ueyama and Deser 2008), and cross checks of surface pressure–based neutral atmospheric delays to the delays measured by space geodetic techniques (Jin et al. 2009).

Aside from these practical advantages, the DW station tide compilation has been shown to be somewhat less coherent than any set of analyst-guided estimates, resulting in usually twice as high root-mean-square (RMS) differences when compared to the mean S_1 and S_2 cycles of numerical circulation models (Table 2 of Ray 2001). DW opted to process all stations with predefined algorithms, which were presumably insensitive to the individual time series characteristics related to large data gaps, time stamping problems, or defective instruments. Figure 1b depicts one repercussion of this strategy in the phase lag plot for the DW gridded S_1 solution; a considerable amount of noise obscures the first-order, circular phase advancement of the main migrating tide, while comparable effects in the amplitude (Fig. 1a) are attenuated by spatial smoothing. Moreover, the secondary S_1 maximum of up to 70 Pa at 40°–60°S can be disputed in light of the reliability of marine reports as well as more recent, lower-amplitude (30 Pa) determinations from global numerical models (Ray and Ponte 2003). Much in the same manner, tidal oscillations near the poles exceed 30 Pa and thus contradict estimates from available pressure observations (Carpenter 1963). This inadequacy, in combination with sizable jumps of the pressure amplitudes at the 180° meridian, suggests a less-than-optimal and apparently noncircular gridding technique (Watson 1999). The associated spectra of zonal wavenumber versus latitude for S_1 and S_2, depicted in Figs. 6 and 7 of Covey et al. (2011), were therefore inconclusive in terms of some minor but now well-documented tidal modes, for example, the stationary diurnal and semidiurnal waves.

3. Data from global atmospheric analyses

Climatological means of the barometric S_1 and S_2 tides from three reanalysis (i.e., constant model) systems and one operational analysis are auxiliary products that will prove useful when discussing our station tide estimates, and particularly when refining parameterizations of the subsequent gridding procedures. The utilized surface pressure fields are subsets of the Interim European Centre for Medium-Range Weather Forecasts (ECMWF) Re-Analysis (ERA-Interim; Dee et al. 2011), the Modern-Era Retrospective Analysis for Research and Applications (MERRA; Rienecker et al. 2011) produced by the National Aeronautics and Space Administration (NASA) Global Modeling and Assimilation Office (GMAO), the newly released Japanese 55-year Reanalysis (JRA-55; Ebita et al. 2011) of the Japan Meteorological Agency, and the operational ECMWF model implemented with a delayed cutoff (DC) window for incoming observations [see Persson (2011) for details]. These datasets are henceforth abbreviated as ERA, MERRA, JRA, and DC. A unified analysis

period 2004–13 was selected with the exception of the DC model, where only 5 years of surface pressure (2007–11) were available. The resulting climatologies of S_1 and S_2 are nonetheless well representative of the expected long-term means since an extension to a 10-yr window usually alters the wavenumber spectrum by less than 1% for the migrating tides and by 10%–15% for harmonics of small signal-to-noise ratio such as the stationary wave signature of 5–10 Pa near the poles.

To overcome the insufficient temporal resolution of the standard analysis output, we resorted to 3-hourly forecasts that are typically initialized at the start of successive analysis cycles every 6 or 12 h. Within JRA, these products are denoted ''instantaneous diagnostic fields'' and MERRA supplies comparable surface pressure data as ''assimilated states,'' both at a prescribed horizontal spacing of 1.25° in latitude and longitude. MERRA achieves smooth transition between all analysis cycles through a specific predictor–corrector scheme (Rienecker et al. 2011). Contrarily, the 3-hourly ERA and DC products, downloaded on an equidistant 0.5° grid, correspond to the first four time steps (3, 6, 9, and 12 h) of successively concatenated 10-day forecasts and might therefore contain small discontinuities at the transitional epochs. Provided that the forecast arcs are free from systematic drifts, the effect of such discontinuities can be largely eliminated by using long-term averages as implemented here. The functional model fitted to the pressure time series at each geographic location (latitude φ, longitude λ) consists of two sinusoids of form

$$S_n = A_n \cos(nt - \phi_n) = a_n \cos(nt) + b_n \sin(nt), \quad (1)$$

where $n = \{1, 2\}$ and t signifies UTC in radians; A_n is the tidal amplitude; and ϕ_n is a phase lag reckoned relative to $t = 0$ and derived from b_n/a_n, that is, the inverse tangent of the harmonic coefficients.

While a more detailed examination of the various pressure tide solutions from all four models would be principally insightful, we are content to accept that some of their differences will emerge in later sections of this paper. It shall be noted, however, that the underlying assimilation systems closely agree in terms of observational data as well as the quality procedures imposed thereupon, and discrepancies in the S_1 and S_2 climatologies are therefore likely to originate from the physical model formulation, its forward integration, and sensitivity to different input data. Native model resolutions vary in some degree, with ERA meshes being the coarsest at approximately 80-km intervals, MERRA and JRA being run at about 60 km, and most of the DC forecasts being produced with a 50-km discretization.

4. Land station and marine observations of air pressure tides

a. Data from the ISPDv2

Pressure observations within the ISPDv2 are classified into three components comprising land stations (including islands and some fixed buoys), marine reports, and data trajectories for tropical cyclones that were excluded from our analysis. The marine component of ISPDv2 corresponds to a present-day version of COADS, and the station archive has been assembled from multiple national and international collections (Compo et al. 2010). We downloaded all available marine and surface pressure data via the National Center for Atmospheric Research (NCAR) Data Support Section for a principal analysis window from January 1990 to December 2010. This period was extended several times in retrospect in an attempt to obtain better global coverage, especially to improve some initially sparsely sampled equatorial regions featuring significant tidal variability. Table 1 summarizes the geographical locations and time frames of the different subsets.

Both marine and station barometric data are arranged in chronological order with each entry tagged by a unique observational ID, positional information of the recording platform, and feedback information coming from the five-step quality-control procedure of the 20CRv2 (Compo et al. 2011). Observations failing these tests of credibility against the variability of neighboring stations and the local background plus error guess of the 20CRv2 Kalman filter ensemble are indicated by a negative ''usability check for reanalysis'' and were dropped in a first processing step. Being somewhat tied to model predictions via the background estimate, it is entirely possible that physically legitimate observations were occasionally rejected during quality control as a result of an inappropriate model evolution, typically when pressure

TABLE 1. Specifications of the surface and marine reports extracted from ISPDv2 for the main analysis window and retrospective extensions denoted A, B, C, D, and E, which are also illustrated in a later section (Fig. 4). Additional data for a small subset of island stations in the Pacific and the central Indian Ocean were pinpointed manually in the databank for the period 1900–90.

	φ range	λ range	Period
Principal analysis window*	90°S–90°N	180°–180°	1990–2010
A: Arctic	70°–90°N	180°–180°	1950–90
B: Antarctic	90°–48°S	180°–180°	1900–90
C: Central Africa	20°S–30°N	5°–60°E	1955–90
D: Amazonas and Andes	20°S–10°N	80°–50°W	1960–90
E: Brazil	25°S–0°	50°–30°W	1966–90

* For both continents and oceans.

changes occur on scales not represented in the 20CRv2 configuration. Indications for such an overcompensation were indeed found for a few selected coastal stations (Greenland) but involve only a small fraction of the full barometer time series at each site. More importantly, the usability check appears to withhold the majority of gross outliers, for example, because of malfunctioning sensors recording anomalous or only default pressure values. Time-tagging problems are particularly apparent for several Russian stations where observations at specific times of the day seem to be frequently ascribed to other epochs in advance; see Fig. 2 for a possible example. In the following, only the raw though quality-controlled ISPDv2 observations, unmodified by any interpolation or assimilation technique, were considered.

Potential perturbations of mean annual S_1 and S_2 components as retrieved below relate to intra- and interannual tidal variability (DW; Covey et al. 2011) and need to be mitigated by using multiyear time series for an integral number of full calendar years (Ray and Ponte 2003). Moreover, diurnal harmonics extracted from SLP reports are susceptible to aliasing effects from imperfect isothermal reduction schemes (Mass et al. 1991), and data from these sensors were categorically rejected if located at altitudes >1 km (Covey et al. 2011). Additional complications arise from frequent data gaps and sampling rates that differ both within each individual time series as well as from one platform to another. Insufficient observation intervals of days or even weeks are not uncommon within the ISPDv2 station component, but the prevailing sampling is at the eight synoptic hours (0000, 0300, 0600, 0900 UTC, etc.), and many of the Japanese and U.S.-based stations also record at hourly intervals. Although this time discretization in principle allows for a treatment of the small terdiurnal surface pressure tide, we abstained from such an attempt for the sake of simplicity.

b. *Analysis of station observations*

The ISPDv2 station ID compilation, as available from Compo et al. (2010), comprises more than 32 000 disjoint entries, which were narrowed to 13 155 IDs based on the requirement of at least 4 years of observational coverage. No prior information on the eventual data frequency at each site was available for this initial reduction. Discarded stations present in any of the regional extensions noted in Table 1 were readopted in hindsight. After allocation of the pressure data to the resulting station listing, a range of constraints had to be imposed on each barometer series to check its principal usability for the problem at hand. The upper threshold for data gaps was set to 20 days in order to enable observation platforms in rather remote places with frequent outages to contribute to an optimal global coverage. In light of such gaps, each station should have at least 3 years of data, which is a sufficiently long duration to obtain reliable annual climatologies of S_1 and S_2 in low and most middle latitudes but might lead to distortions from interannual variations in polar and subpolar regions [Fig. A1 of Covey et al. (2011)]. In a final screening step, we judged the approximate data frequency by aid of the record length. Stations falling short of 5000 samples indicate an average sampling interval greater than 6 h over 3 years and were dropped.

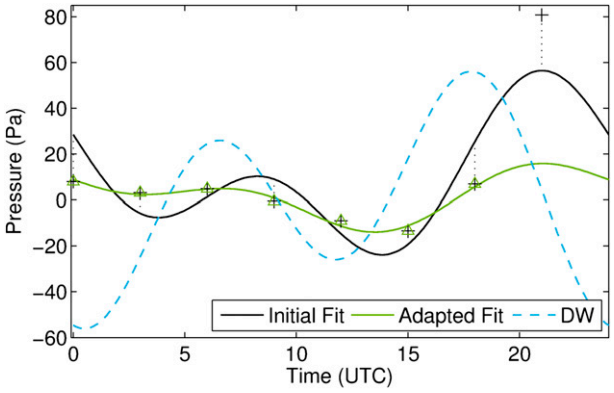

FIG. 2. Fit of pressure tide harmonics at station Teriberka (φ = 69.20°N, λ = 35.10°E), Murmansk Oblast, Russia, based on two different mean day composites obtained from 1) applying the standard constraints as given in the text, that is, n_e = 500 observations (black crosses) and 2) choosing $n_e > 930$ (green triangles). The mean annual DW tide at this location (dashed blue curve) is of doubtful magnitude for subpolar latitudes (40.3 Pa in S_2).

Our method of deducing tidal harmonics followed Mass et al. (1991) in averaging pressure values that occur at the same time of the day. This ''stacking'' to a daily mean composite is equivalent to a discrete Fourier transform for the case of equidistant time series and allowed us to introduce two additional quality checks. First, only epochs holding an adequately large observational count n_e were retained in order to prevent infrequently sampled epochs to distort the subsequent fit of tidal harmonics. The chosen threshold n_e = 500 is about 50% of the highest possible number of observations for any specific epoch over the course of 3 years (3 × 365 = 1095 samples). Second, we required at least six epochs, three of them each half-day, to pass all test criteria and supply the observables for the least squares adjustment obeying Eq. (1), plus a daily mean pressure.

Applied to the raw barometric data without further alteration, the screening and harmonic decomposition procedure resulted in a sizable amount of S_1 and S_2 determinations that were either suspicious in light of the tidal variability implied by neighboring stations or simply implausible given our approximate knowledge of the global pressure tide behavior. Closer inspection of these cases as well some seemingly accurate stations suggested

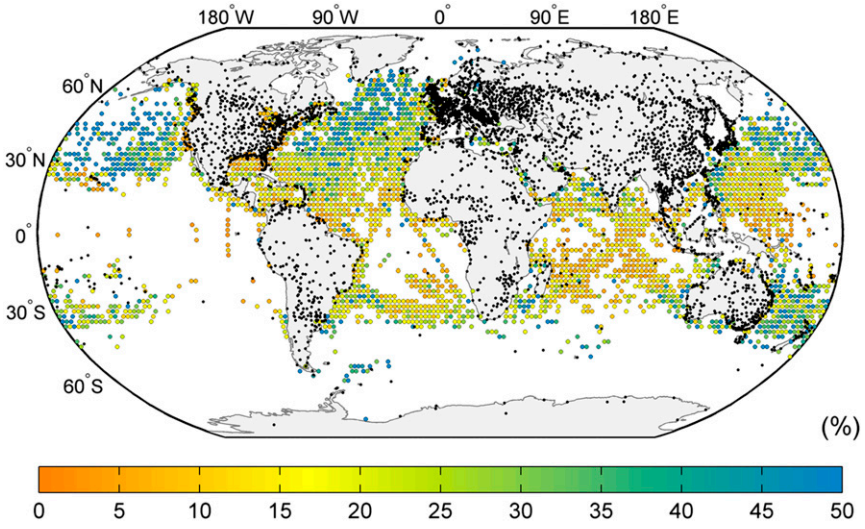

FIG. 3. Locations of 3970 ground truth stations (small black dots) and 2924 ocean boxes (colored circles) where both S_1 and S_2 pressure tides were determined from the quality-controlled ISPDv2 data mainly during 1990–2010. The color code of the marine points illustrates the standard error of unit weight from the harmonic fit, expressed as percentage relative to the combined S_1 and S_2 amplitude. Values at ocean boxes holding only six composite epochs, that is, a low degree of freedom, were manually set to 50%.

that the individual characteristics of all barometer series were too diverse to be universally accounted for by a predefined set of screening parameters. Hence, we adopted the aforementioned constraints as minimum requirements to eliminate suspect stations in advance and we allowed them to be tightened elsewhere. Most of these local refinements were based on the observation count n_e per epoch, an example of which is given in Fig. 2 for station Teriberka, Murmansk Oblast, Russia, where the initial mean day fit to an eight-epoch sample is "levered out" by a dubiously high 2100 UTC average of 80 Pa. Increasing n_e to values greater than 930 removes this obvious anomaly and leads to a harmonic fit that closely approximates all other data points and is of credible magnitude (10 Pa) for subpolar regions. Persistent jumps at 2100 UTC in the underlying time series of Teriberka are visible throughout the analyzed period June 1995–June 2000 and 48% of the ~1800 observations at this time of the day are in fact withheld by the ISPDv2 usability check. A fair number of minor outliers appear to remain undetected, though, and likely affect the 2100 UTC average in Fig. 2. Overall, the correct choice of parameters at nearly 7000 sites fulfilling the minimum requirements could only be made manually, by plotting the observables, judging the first guess fit, and fine-tuning the initial constraints if necessary.

The network of 3970 continental and island barometers retained after manual inspection, shown in Fig. 3, is largely equivalent to the DW station compilation, except for a modest densification achieved by aid of our extended analysis windows over Brazil and central Africa, as well as a sparser though noncritical coverage of Eurasia. The median time series length computed from all 3970 stations is 7 years, and the longest two records span 41 years (Midway Islands, North Pacific Ocean) and 22 years (Jacareacanga, Amazon River basin); short durations of 3 or 4 years occur for about 25% of all sites, and only 146 SLP stations reside above 300 m. As envisaged, the internal consistency of the dataset surpasses that of DW, apparent, for instance, from the globally averaged RMS differences of S_1 or S_2 cycles at any two neighboring stations within a specified distance (Table 2). Using a scan radius of 200 km, the global mean RMS of the diurnal tide drops from 27.7 Pa in DW to 11.6 Pa in the present compilation, and the semidiurnal consistency check is likewise bettered from 21.2 Pa to a level of 7.1 Pa, even though DW's results should be, in principle, much more affected by a low-magnitude bias due to intense clusters prevailing in Europe and Southeast Asia. The quoted statistics were found to be highly robust across a broad range of search radii.

c. *Analysis of marine observations*

Infrequent subdaily pressure recordings over the oceans originate from ships and buoys that do not have fixed locations. The ISPDv2 marine data covering 1990–2010 were therefore screened sequentially and binned to cells of size 2° × 2°. Each of these ocean boxes might thus hold multiple observations at the same epoch with inherent phase disparities being as large as 2° or 8 min at

TABLE 2. Internal consistency of the station and marine tide compilations from DW and this study judged on the basis of RMS differences (Pa) between neighboring points. Similar comparisons in Ray (2001) have been performed by computing RMS measures over a global sample of differences without mapping stationwise RMS values to their mean.

Component (search radius)	Dataset	S_1 (p_s)	S_2 (p_s)	Station pairs
Land stations	DW	27.7	21.2	64 723
(200 km)	This study	11.6	7.1	14 445
Ocean boxes	DW	29.1	30.4	3056
(300 km)	This study	12.1	14.6	6317

the diurnal cycle. In an attempt to also retrieve tidal coefficients for areas with little maritime traffic, we adopted considerably relaxed constraints on the pressure time series and their mean day composites. Trial and error computations yielded a minimum of 500 samples ($n_e = 50$ accordingly) over a duration of at least 3 years granting data gaps of up to 100 days. As a consequence, the reliability of the S_1 and S_2 harmonics is far less than that of the station data, and distortions from unresolved tidal time variability must be accepted.

An otherwise analogous processing to section 4b resulted in a network of 2924 ocean boxes assembled along or in the proximity of major ship routes (Fig. 3). The coverage of the entire Atlantic and Indian Oceans, as well as the northern and western Pacific, is fairly good, but almost no data points could be retained for the east Pacific Ocean, the Arctic Ocean, and subantarctic regions. Dissimilarities to the rather uniform DW ocean box distribution presumably arise from differences in data processing and DW's supplemental use of 6-hourly marine reports. We conducted internal consistency checks of both datasets in the same fashion as for the land portion in Table 2 after widening the maximum pairing distance to 300 km. The global mean RMS differences at 12.1 (S_1) and 14.6 Pa (S_2) for the newly compiled marine network are again better than the weak internal agreement of the DW data (~30 Pa), even though a clear deterioration with regard to the land component must be conceded (especially considering the small amplitude of the diurnal tide over the oceans). Figure 3 highlights the likely positions of many of these less credible marine points by an additional color code, gauged to the amplitude-normalized standard error of unit weight from the harmonic fit at each location. Thirty percent of all ocean boxes, mostly those at middle and higher latitudes, feature standard errors larger than 30% of the combined S_1 and S_2 amplitude and thereby attest to a considerable scattering among the stacked observables. Estimates from these locations may thus be unrepresentative of the actual tides.

d. *Subsetting and comparison with global analysis tide data*

Many of the station tide determinations in densely sampled midlatitudes provide redundant information that is of no particular benefit in computing air pressure tide climatologies on a global grid. We therefore subsampled the original network in Fig. 3 using the condition of maximal one station or ocean box per 1.5° × 1.5° cell. Land stations were preferred to marine data, and in case of conflicts, we selected the longest observing site, believed to also hold the most reliable tidal harmonics. This data thinning, preserving 2651

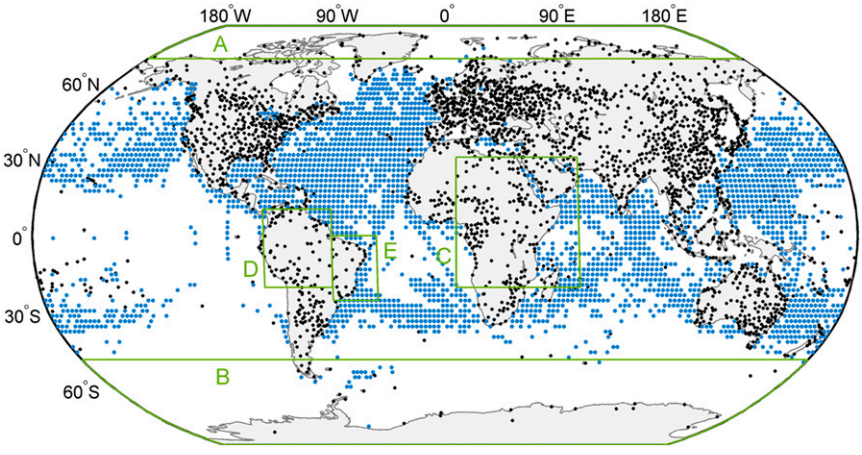

FIG. 4. Subset of the initial in situ network obtained after data thinning to equidistant cells of size 1.5°. The preserved 2651 land stations (black dots) and 2686 ocean boxes (blue dots) are displayed together with the location of data supplements A, B, C, D, and E as introduced in Table 1 and provide the $N = 5337$ observations used for fitting S_1 and S_2 harmonic coefficients to a uniform 1° grid in section 6.

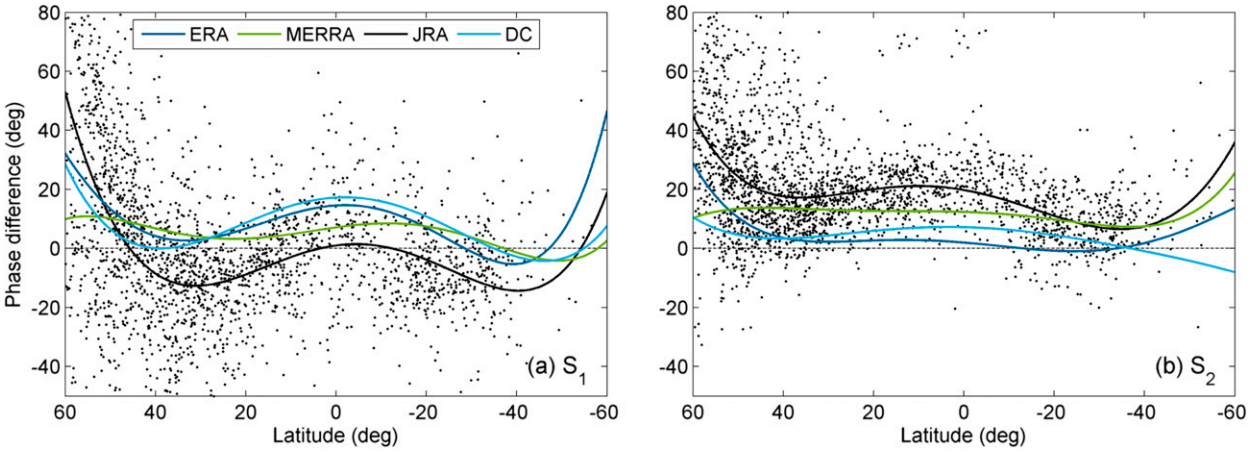

FIG. 5. Differences in (a) S_1 and (b) S_2 Greenwich phase lags between the model-implied tides and the estimates of 2651 land stations as included in the subsampled compilation (Fig. 4). Pointwise differences are plotted for JRA (black dots), along with least squares adjusted fifth-order polynomials (black curves). For ERA (dark blue), MERRA (green), and DC (light blue), only the low-degree polynomial fits are shown.

of the original 3970 station barometers without any noticeable degradation of the spatial coverage (see Fig. 4), is thus likely to further aid the quality of our in situ network.

An initial comparison of the $N = 5337$ (2651 land, 2686 oceanic) subsetted estimates with global analysis tides disclosed small systematic biases in the phase of the S_2 tide as deduced from MERRA and JRA. Phase lag differences $\Delta\phi$ for both models are plotted in the sense of model minus station across latitude in Fig. 5b with a restriction to land points to sidestep the considerable spread from less reliable ocean box data. By aid of least squares fitted fifth-order polynomials, fairly robust offsets with median values of $\overline{\Delta\phi} = 11.2°$ (MERRA) and $\overline{\Delta\phi} = 18.8°$ (JRA) can be obtained, whereas analogous estimates for ERA and DC are much smaller and probably below the level of statistical variability of the experiment. While the causes for such systematics remain obscure, their correction in the model fields by a simple phase lag surcharge $\overline{\Delta\phi}$ at all grid points (Ray 2001) is essential, and only corrected S_2 phases were used for the remainder of this study. A similar test of the various S_1 fields, illustrated in Fig. 5a, proves to be inconclusive but is likely impaired by regional inadequacies of our station tide estimates; see the persisting "cusp" of $\Delta\phi$ in the tropics.

Root-mean-square values of the differences between station and global analysis S_1 and S_2 tides, given in Table 3 as global averages over all locations of the reduced land plus ocean merger, are in the range of 12–16 Pa throughout and only moderately exceed the agreement achieved by Ray and Ponte (2003) for their individually analyzed station data (see the table notes for a remark on the comparability of this study). In fact, the statistics in the semidiurnal band would be further improved (toward ~11 Pa in RMS) if it were not for the inclusion of the

TABLE 3. RMS differences (Pa) of ERA, MERRA, JRA, and DC with the S_1 and S_2 estimates of the subsampled compilation shown in Fig. 4. Results for the model combinations MERRA–JRA and ERA–DC are not included but do not deviate significantly from the tabulated values. Comparable RMS statistics published by Ray (2001) and Ray and Ponte (2003) do not derive from averages over all stations but instead from the globally merged field of scattered differences in a_n and b_n. If adapted to this convention, our S_1 and S_2 RMS values would amount to 15–18 Pa in the table.

	S_1 (p_s)			S_2 (p_s)		
	All stations	Land	Oceans	All stations*	Land	Oceans
In situ–ERA	13.7	15.5	11.9	14.4 (—)	11.2	17.5
In situ–MERRA	12.3	14.4	10.2	14.7 (15.2)	11.5	17.8
In situ–JRA	13.7	16.9	10.6	15.6 (17.4)	12.7	18.5
In situ–DC	12.9	15.0	10.9	12.3 (—)	10.2	14.5
ERA–MERRA	7.9	9.1	6.7	9.0 (14.6)	9.1	8.9
JRA–ERA	10.4	12.8	8.0	11.4 (19.2)	11.7	11.1
MERRA–DC	7.9	8.9	6.8	8.7 (10.0)	9.0	8.4
JRA–DC	10.5	13.5	7.6	11.4 (14.9)	11.9	10.9

* Values before phase correction in parentheses.

markedly less reliable oceanic subset (RMS ~ 18 Pa). The phase adjustment imposed on MERRA and JRA slightly improves their consistency to the in situ predictions but, interestingly, it also yields a significantly better agreement of all analysis-based S_2 tides among themselves; see the model-to-model comparisons in the bottom half of Table 3. At continental and island sites, these intermodel RMS values amount to 9–12 Pa and are very comparable to the station-to-model statistics (10–13 Pa). For the diurnal tide, however, in situ estimates for both land and oceanic points are in less good agreement with models, with respective RMS differences roughly 3 Pa greater. Whether this implies larger errors in the station data or the models is not obvious; if the former, then the global S_1 climatology deduced in the following section will be less accurate than long-term averages from present-day analysis systems. On the other hand, these RMS differences could be pointing to common systematic errors in models for which the station estimates may eventually furnish clues.

5. Multiquadric fit

a. Interpolation technique

Nuss and Titley (1994) illustrated the excellent usability of multiquadric interpolation to fit scattered pressure data to an arbitrarily chosen uniform grid. We adapted their equations for geographical coordinates on the sphere, assuming that $N = 5337$ observations H_j, that is, the field of tidal components a_n or b_n for either $n = 1$ or 2, satisfy the interpolation equation (in matrix notation):

$$\mathbf{H}_j = [\mathbf{Q}_{ij} + l\delta_{ij}]\boldsymbol{\alpha}_i, \quad i,j = 1, \ldots, N. \tag{2}$$

Here, l is an appropriately chosen smoothing factor, δ_{ij} denotes the Kronecker delta, and $\boldsymbol{\alpha}_i$ accommodates the unknown weighting factors of the (dimensionless) hyperboloid radial basis function Q_{ij} expressed in terms of the geodesic distance s_{ij} between points i and j:

$$Q_{ij} = -\left(\frac{s_{ij}^2}{c^2} + 1.0\right)^{1/2}. \tag{3}$$

Nuss and Titley (1994) gave a coherent recipe of how to invert the linear system in Eq. (2) to any target grid and also elucidated the relevance of the method's two "shape parameters" embodied by c and l. Specifically, smoothing via $l\delta_{ij}$ (a simplified version of the originally suggested scheme) accounts for observational uncertainty and circumvents numerical instability. In contrast, the multiquadric parameter c regulates the curvature of the basis functions, with sharp gradients (small c) needed to delineate the local features of the S_1 tide over continents and comparatively large c values being required to capture the more regular nature of the global S_2 tide; see the next section for objective choices for both c and l. Our computational implementation of the multiquadric fit rests upon a global $1° \times 1°$ grid, adopted to guarantee a reasonably good distinction between pelagic and land points as well as a realistic representation of the continental diurnal tide "leaking" across coastlines (e.g., at the East African coast; see Fig. 8 of Ray and Ponte 2003). To speed up calculations, in particular for densely sampled regions of low tidal amplitudes, the interpolation to any target grid point was carried out based on the nearest 50 observations. This modification entailed no apparent degradation with respect to the strict solution using the full network.

b. Determination of shape parameters for S_1 and S_2

The adopted interpolation technique allows for regionally varying choices of both c and l, and such flexibility is in fact warranted for the diurnal pressure tide in light of its different appearance over landmasses and oceans owing to the variable action of turbulent sensible heat transport. The preferable combination of c and l for each of these interpolation runs (S_2 global, S_1 land, S_1 ocean) might be determined by trial and error calculations and visual inspection, but a less subjective approach is desirable. The K-fold cross validation (e.g., Stone 1974), based on partitioning the data into K interchangeable subsets of training and test data, fixes c and l solely according to the in situ estimates, but we found some initial test calculations largely unsuccessful. We therefore chose to calibrate the shape parameters based on a station tide scatter "simulated" from global analysis fields. In brief, tidal components a_n and b_n were extracted at the N in situ locations from the climatologies of ERA and perturbed by a realistic amount of random noise to mimic the uncertainty contained in the actual ground truth data. Repeated multiquadric interpolation of this scatter to carefully selected test areas, as specified in Table 4 together with the superimposed noise levels, yielded different gridded solutions for varying c–l pairings, which were finally xamined for their agreement with the original ERA tides at grid cells that did not hold any station observations (approximately 90% of all cells for each test area). Similar control runs were conducted for simulated station tide observations from MERRA and JRA for comparison.

1) Calibration of the S_2 tide

The test area for adjusting the semidiurnal interpolation parameters involves Indonesia, Australia, and the east Pacific Ocean (Fig. 6), accommodating both densely and

TABLE 4. Spatial coverage of the three test areas used for calibrating the shape parameters of the global S_2 tide and the S_1 tide over land and oceans. The noise levels (Pa) superimposed on the ERA-based scatter conform to the central tertiles of the merged, absolute RMS differences |ERA − MERRA| ∪ |ERA − JRA| ∪ |ERA − DC| at the in situ locations of each test area.

	S_2	S_1 land	S_1 ocean
φ range	35°S–25°N	25°–3°S	20°S–25°N
λ range	105°E–135°W	67°–38°W	160°E–135°W
ERA noise interval, a_n	6.2–13.3	5.6–12.0	1.6–3.7
ERA noise interval, b_n	5.3–10.7	9.2–19.3	4.5–6.8

sparsely sampled regions with sufficiently distinct spatial variability in S_2. Noise surcharges on the ERA-based scatter of a_2 and b_2 were deduced from the interagreement of all analysis tide models at the depicted locations of 855 land and oceanic points. In detail, we merged absolute RMS values of the three sets of residuals, ERA–MERRA, ERA–JRA, and ERA–DC, to one single distribution and extracted upper and lower class limits of the resulting central tertiles (6.2–13.3 Pa for a_2 and 5.3–10.7 Pa for b_2; see Table 4). Perturbations of a_2 and b_2 were then allowed to vary randomly within these intervals with arbitrary signs. This strategy ensured an increased independence of the simulated ERA scatter from the model and also eschewed unrealistic and numerically critical smoothing parameters in the vicinity of zero (singularity typically appears for $l \sim 10^{-4}$).

We judged the predictive performance of every c–l pairing by confronting its respective gridded solution to the initial ERA S_2 tide in terms of RMS differences at each 1° cell void of in situ observations. The local RMS values were mapped (averaged) to a test area mean and the experiment was repeated 10 times for all c–l combinations to gain some robustness. Results for this minimization approach are displayed in Fig. 7 and suggest optimal parameter values of $c = 0.50$ and $l = 0.025$, which were further substantiated by our control runs; see Table 5 for the case of MERRA. Considering that the mean S_2 amplitude in the test region exceeds 100 Pa, the attained minimum RMS of 3.3 Pa is encouragingly low (though nonzero) and testifies to the excellent applicability of multiquadric interpolation for the problem at hand. On a side note, gridded S_2 fields provided by shape parameters within the 0.5% contour are visually indistinguishable.

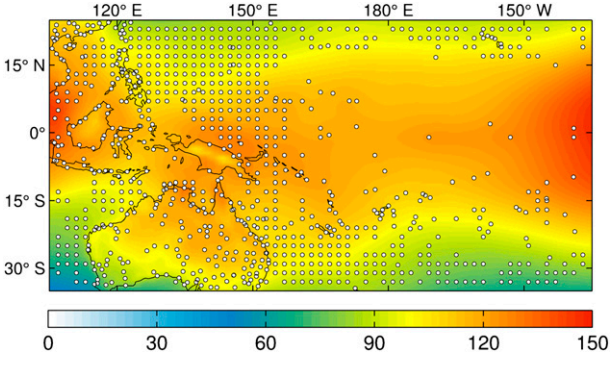

FIG. 6. Test area for determining the shape parameters of the semidiurnal tide interpolation. The white dots indicate the locations of 855 ground truth estimates used for obtaining the noise intervals in Table 4; the color map illustrates the S_2 pressure amplitude (Pa) as contained in the ERA climatology from 2004 to 2013.

2) CALIBRATION OF THE S_1 TIDE

Appropriately selected test areas allowing for disjoint land–ocean calibration experiments in the diurnal band are illustrated in Fig. 8. Judging from the ERA climatology, the snippet in the tropical Pacific accommodates tidal oscillations that are dominated by the weak migrating S_1 wave and only occasionally interrupted by modulations arising at islands. By contrast, the continental sample region covers large parts of Brazil, Bolivia, and Paraguay and supplies smaller-scale but significant tidal variability in the range of 20–190 Pa. Accordingly, the superimposed noise levels—once more calculated from the central tertiles of ERA RMS differences with all other analyses at the in situ locations—are moderate (<7 Pa) over the oceans (132 test points) but may reach 19.3 Pa over land (51 test points; see Table 4).

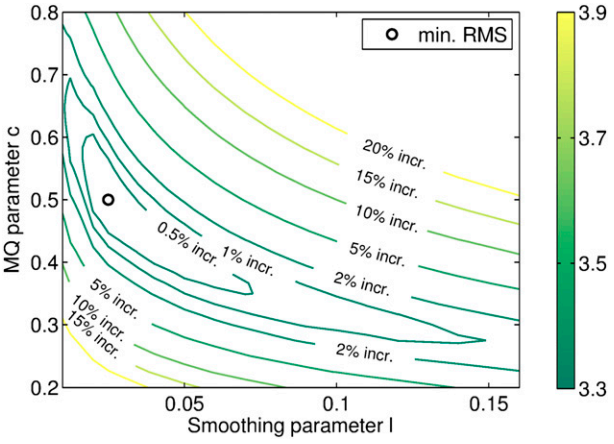

FIG. 7. Calibration of the semidiurnal interpolation parameters c (in radians) and l using the test area in Fig. 6. Results expressed as regionally averaged RMS difference (Pa) between the unperturbed ERA S_2 tide and that recreated from multiquadric interpolation; see the text for further explanation. Contours signify the increase of RMS values in percentage relative to the absolute minimum (black circle) at 3.3 Pa. Gridded solutions based on large values of c and l (e.g., $c = 0.60$, $l = 0.10$) appear to be too smooth, while predictions in the lower left corner entail obvious artifacts such as ''grainy'' pressure patterns.

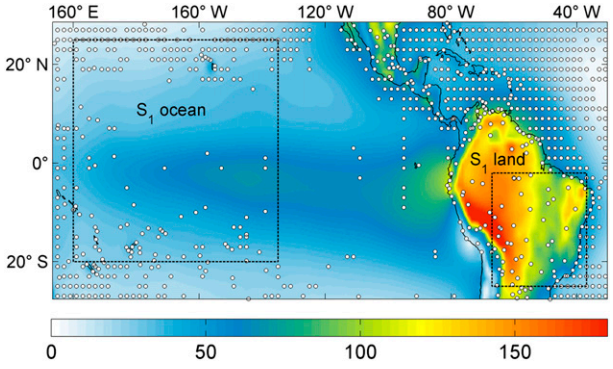

FIG. 8. Test areas for determining the shape parameters of the diurnal tide interpolation over land and oceans (black dashed boxes). The white dots inside the boxes indicate the locations of 51 and 132 ground truth estimates used for obtaining the diurnal noise intervals in Table 4; the color map illustrates the S_1 pressure amplitude (Pa) as contained in the ERA climatology from 2004 to 2013.

Averaged RMS results in Fig. 9 were obtained in the fashion of the previous section from the tenfold calibration of each c–l combination against the S_1 climatology of ERA. Both experiments for land and oceanic areas showcase the need for considerable smoothing in the proximity of $l = 1.0$, while the optimal values for c (0.024 and 0.070, respectively) are markedly different as anticipated above. The achieved minimum RMS for the continental S_1 tide at 8.4 Pa is less than 8% of the mean test area amplitude (110 Pa) but still exceeds the respective postfit values (roughly 3.0 Pa) of the other two calibration efforts. This attests to the comparatively poor performance of the interpolation method in recreating the strong local diurnal pressure variability from sparsely distributed observations. Table 5 summarizes the final parameter combinations for S_1 and S_2 based on the calibration results from ERA. Analogous computations using the scatter and noise levels of MERRA are consistent with these c–l values and indicate that their determination was accomplished in a largely model-independent way. The somewhat coarser deviation in the prediction of l for the diurnal pressure tide over the oceans most probably relates to the slightly enhanced magnitudes in the random distortions of b_1 for ERA. By visual inspection of the related S_1 fits, we judged the smoother solution produced by $l = 1.30$ to be more realistic.

6. Pressure tide climatologies

a. *Global maps of* S_1 *and* S_2

Mean annual components of the barometric tides, gridded to a regular 1° mesh by aid of the optimized interpolation parameters in Table 5, are displayed in Figs. 10 (S_1) and 11 (S_2). In situ scatters of the two tidal components a_n and b_n were adjusted separately and then combined to yield amplitude and phase grids. For the purpose of distinguishing continental and pelagic stations in the interpolation of the S_1 tide, we used a global land–sea mask at 0.5° resolution and thereby allocated small, subgrid-scale islands to the oceanic subset of the fit. RMS differences of the inferred empirical models with the observational data, computed by analogy with Table 3, are 8.1 (S_1) and 8.9 Pa (S_2) on average for all 5337 ground truth locations. Expressed as normalized errors relative to the individual station tide amplitudes, these values correspond to 0.32 and 0.14, with the diurnal cycles being affected by a considerable stochastic variability among

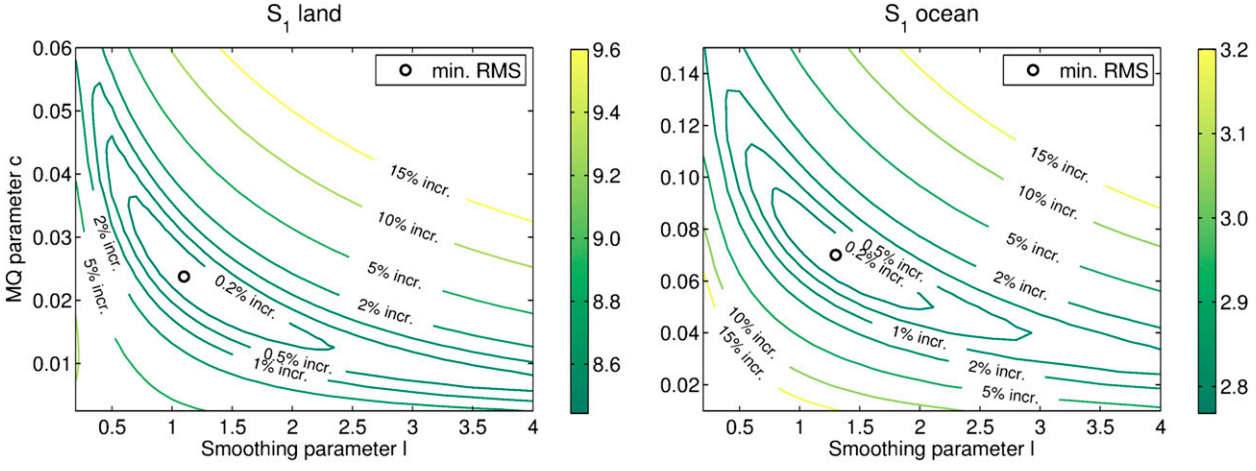

FIG. 9. Calibration of the diurnal interpolation parameters c and l over (left) land and (right) oceans using the test areas in Fig. 8. Results expressed as regionally averaged RMS difference (Pa) between the unperturbed ERA S_1 tide and that recreated from multiquadric interpolation. Contours signify the increase of RMS values in percentage relative to the absolute minima (black circles) at 8.4 and 2.8 Pa, respectively.

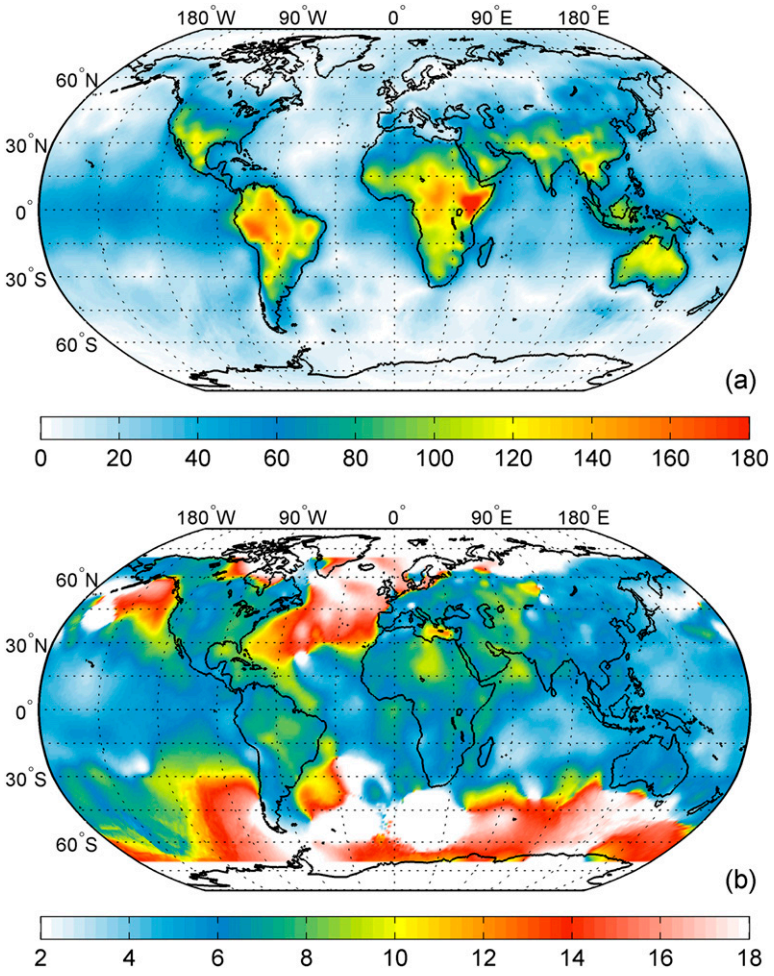

FIG. 10. (a) Diurnal surface pressure amplitudes (Pa) and (b) LST of maximum pressure T_{max} (h) as obtained from multiquadric interpolation of 5337 station tide estimates. The relation to the diurnal Greenwich phase lag ϕ_1 (rad) is $T_{max} = (\phi_1 + \lambda)(24/2\pi)$.

the S_1 estimates from ocean boxes. Respective statistics between global analyses tides and the new gridded solutions—denoted MQI following our use of multiquadric interpolation—are slightly inferior (by about 5%–10%), as one would expect. On a positive side note, the agreement of MQI and ERA does not persistently surpass those of other model combinations and thereby rebuts any speculation that a bias toward ERA has been incurred during calibration of the MQI shape parameters.

TABLE 5. Results of the calibration experiments for the multiquadric and smoothing parameters c and l based on simulated scatters from both ERA (in bold) and MERRA (in parentheses).

	S_2	S_1 land	S_1 ocean
c	**0.50** (0.50)	**0.024** (0.022)	**0.070** (0.065)
l	**0.025** (0.025)	**1.10** (1.40)	**1.30** (0.80)

Figures 10 and 11 exhibit a level of detail that is unmatched for single station–based models of barometric tides. The S_1 patterns over continents closely resemble those obtained by Ray and Ponte (2003) from ECMWF operational data, and the transition of tidal maxima to the subdued diurnal variability over the oceans is particularly well captured; see, for example, the 40–60-Pa belt encasing most of the landmasses in midlatitudes (Fig. 10a). Owing both to the 1° mesh and our avoidance of postfit smoothing, local peak amplitudes of S_1 for central and East Africa (200 Pa across Somalia and Ethiopia), Peru (165 Pa), the eastern Tibetan Plateau, northern Australia, and the Rocky Mountains (roughly 120 Pa) exceed the respective DW predictions (Fig. 1a) by several tens of pascals. DW's secondary maximum in the southern oceans cannot be confirmed due to our data shortage between 40° and 60°S, but their strong polar oscillations that exceed 30 Pa

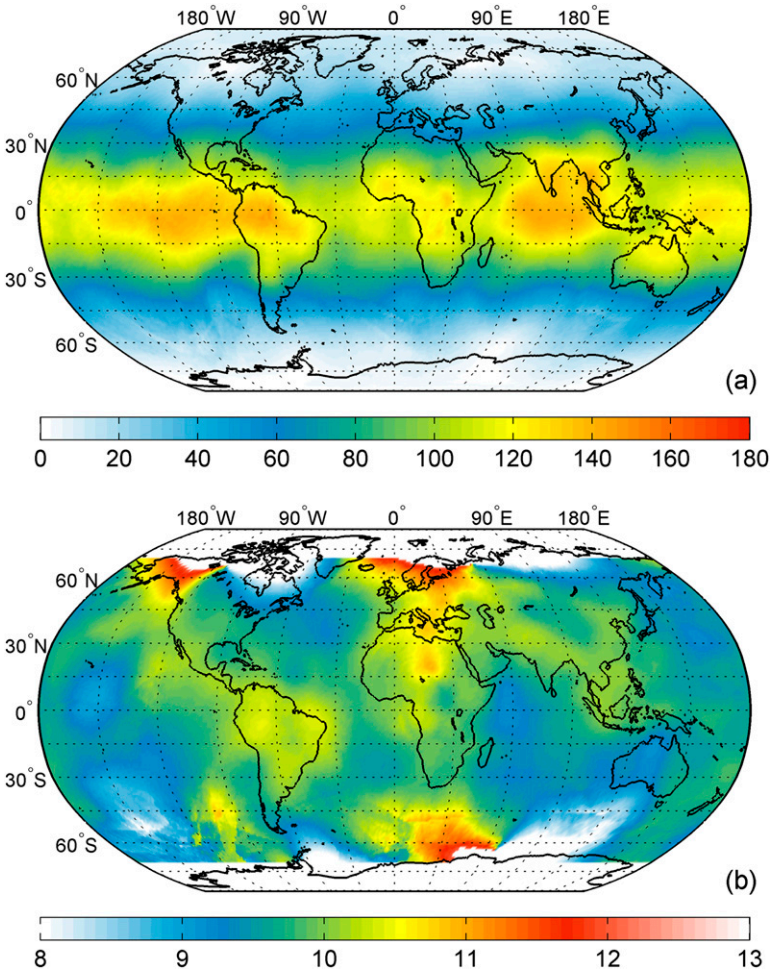

FIG. 11. (a) Semidiurnal surface pressure amplitudes (Pa) and (b) LST of maximum pressure T_{max} (h) as obtained from multiquadric interpolation of 5337 station tide estimates. The relation to the semidiurnal Greenwich phase lag ϕ_2 (rad) is $T_{max} = (\phi_2 + \lambda)(12/2\pi)$.

are certainly refuted. The corresponding phase plot, expressed as local solar time (LST) of maximum pressure in Fig. 10b, is spatially coherent with little noise except in regions of very small amplitude and no data; it illustrates a clear zonal dependency of the diurnal phase over the oceans, while almost all continents protrude with peak times T_{max} in the range of 0500–0800 LST. These values contrast to DW by a phase advance of about 1–2 h but comply excellently to findings from dedicated regional studies, for example, T_{max} = 0530–0800 LST over the United States (Li et al. 2009) or T_{max} = 0600–0730 LST for Australia (Kong 1995).

Disparities of the MQI climatologies to the DW model are somewhat less drastic for the S_2 tide (Fig. 11), even though a persistent enhancement of peak amplitudes from 130 Pa in DW (their Fig. 8) to 140–145 Pa over the east Pacific Ocean, the Amazon Basin, and the tropical Indian Ocean can be noted. Our result is longitudinally less symmetric than existing spherical harmonic expansions (e.g., Ray 2001), with spatial irregularities being in encouragingly close agreement with a recent free-running forward integration of Hamilton et al. (2008). Nonetheless, very small scale disruptions in zonal symmetry, such as the significant amplitude drop induced by wave scattering at the western Andean slopes (Hamilton et al. 2008), can be only resolved in outlines. Local time phases (Fig. 11b) are almost exclusively 0900–1030 (or 2100–2230) LST throughout the world, displaying only a moderate earlier appearance of the semidiurnal tide over the oceans. The multiquadric method works particularly well in locating the amphidromes of S_2 in Nenetsia (Russia) and the Northwest Territories (Canada), which are obscured in the DW dataset. Our approximate value of 66°N, 112°W for the Canadian amphidromic point corresponds

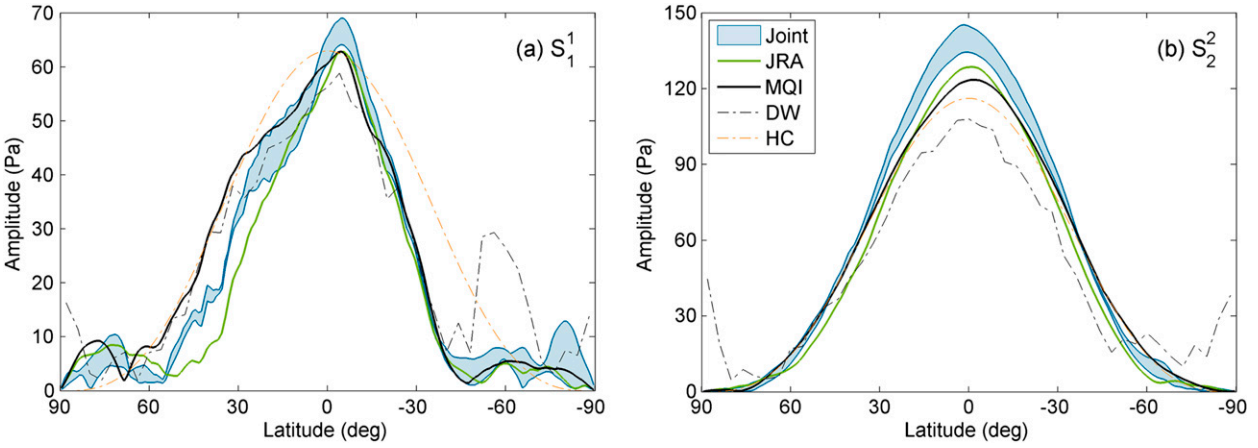

FIG. 12. Latitudinal distributions of the main migrating (a) diurnal S_1^1 and (b) semidiurnal S_2^2 waves in terms of amplitude (Pa). Results displayed for a joint "model" encasing ERA, MERRA, and DC (blue transparent area); for JRA (green curves); the newly derived climatologies of the present paper (MQI, black solid curves); the DW model (black dash–dot curves); and the analytical approximation of Haurwitz and Cowley (1973) (orange dashed curves). Note that comparable wavenumber decompositions of the DW dataset in Covey et al. (2011, 2014) have been apparently downweighted by a factor of $\sqrt{2}$. Slight dissimilarities of the DW profiles to those presented in the DW paper presumably arise from differences in the harmonic analysis procedure.

well to that of Hamilton (1980a) (64°N, 110°W). Additional regional comparisons of the deduced climatology with the S_2 contours obtained by Mass et al. (1991) (United States) and Kong (1995) (Australia) confirm that individual north–south gradients have been captured in a credible manner.

Alternative global S_1 and S_2 charts, as obtained by DW's method of natural neighbor interpolation (Watson 1999), are shown and briefly discussed in the online supplemental material. These plots additionally disclose how multiquadric interpolation acts to smooth out remaining outliers and inconsistencies of our ground truth dataset.

b. Zonal wavenumber decomposition

Fourier analysis of the gridded, complex-valued tidal components $a_n + ib_n$ along circles of constant latitude yields two-sided harmonic representations of the tides as a function of latitude and the zonal wavenumber count s. Applied to the S_1 and S_2 maps of MQI, DW, and all global analysis models treated in this study, these wavenumber decompositions are dominated by the migrating components allocated to either $s = 1$ (diurnal tide) or $s = 2$ (semidiurnal tide). The latitudinal amplitude distributions of these modes, conventionally denoted S_1^1 and S_2^2 with s added as superscript, are shown in Fig. 12 together with Haurwitz and Cowley's (1973) simple analytical expressions based on their observational data. Profiles for ERA, MERRA, and DC exhibit close agreement and were grouped into one enveloping area for reasons of comprehensibility.

The S_1^1 wave of the newly derived empirical model matches the results from global analysis systems flawlessly except for a persistent enhancement of 5–10 Pa between 30° and 60°N. Considering that this zonal belt is in fact amply covered by ground truth estimates and that similar signal structures persist for DW as well as the Haurwitz and Cowley (1973) expansion, this "anomaly" might eventually pinpoint inadequate representations of the main migrating diurnal tide in numerical circulation models. Peak amplitudes in Fig. 12a are found at 4°S throughout, with the MQI model (62.8 Pa) being noticeably closer to the cusps of analysis tides than the annual mean S_1^1 wave of DW (58.8 Pa). Other than that, Haurwitz and Cowley's (1973) assumption of a simple trigonometric latitude dependency ($\sin^3\varphi$) appears to be insufficient in view of obvious hemispheric asymmetries in S_1^1, and none of the utilized sources in fact verifies the large amplitude predictions of DW for migrating tides at the poles and near 60°S.

Long-term means of S_2^2 in Fig. 12b are of distinct symmetry complying closely to a scaled $\sin^3\varphi$ polynomial. This contrasts to DW's finding of a more complicated latitudinal behavior, but their conclusion was quite likely impaired by noise and inconsistencies in the underlying data. More to the point, the actual value of the S_2^2 peak from ground truth estimates is of potential interest for the atmospheric modeling community. Simulations of the atmospheric circulation and the global climate are well known to overestimate semidiurnal surface pressure oscillations with respect to observational determinations as a result of artificial upper model boundaries producing spurious S_2 reflections and subsequent wave enhancements in lower altitudes (Hamilton et al. 2008; Covey et al. 2011). Supposing a median S_2^2 peak of 150 Pa for the most recent database of climate models (Covey et al.

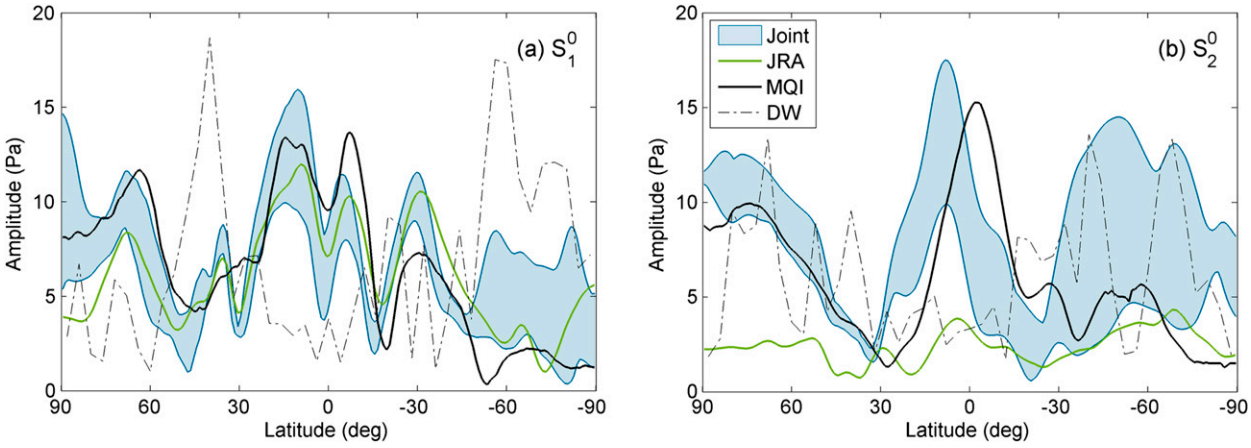

FIG. 13. Latitudinal distributions of the stationary (a) diurnal S_1^0 and (b) semidiurnal S_2^0 waves in terms of amplitude (Pa). Results displayed for a joint "model" encasing ERA, MERRA, and DC (blue transparent area); for JRA (green curves); the newly derived climatologies of the present paper (MQI, black solid curves); and the DW model (black dash–dot curves). All profiles bar DW have been moderately smoothed by a 5-point running average filter.

2014, their Fig. 3), the excess compared to the usually cited empirical data of Haurwitz and Cowley (1973) (116.1 Pa peak) and DW (107.9 Pa) is about 35%, but shortens to 22% if our MQI model (123.4 Pa peak) is adopted as a new observational gauge. Further significant mitigations of this disparity on the side of the observed tide are, however, unlikely, since the assembled in situ compilation—being both comprehensive and of adequate quality—simply does not support higher-amplitude S_2 oscillations at low latitudes (the fraction of 1826 land and/or ocean points within 20°S–20°N holding tidal amplitudes greater than 135 Pa is no more than 20%). Figure 12b reveals less but presumably still significant inconsistencies to observations for assimilation models (130–145 Pa peaks, corresponding to a 5%–18% overestimation), which are constrained to pressure reports and other data.

Stationary tides S_1^0 and S_2^0 isolated from the wavenumber spectra at $s = 0$ are shown in Fig. 13 for all models examined in this paper. Interest in these small harmonics arises from their ability to excite zonal variations in Earth's rotation (Schindelegger 2014) and from the fact that they constitute the sole tidal perturbations at the poles. While Haurwitz and Cowley's (1973) early expansion was clearly supportive of their existence, subsequent confirmations by the DW dataset were precluded by noise and artifacts (Fig. 13). In contrast, signatures of S_1^0 and S_2^0 in the MQI model are of unambiguous integrity, matching the joint ERA–MERRA–DC curve in almost every department. Larger model spreads appear for southern latitudes beyond 40°–50°S, and this is also where the MQI solutions fall short in accuracy owing to lack of observational data. Values at the south polar cap are particularly minute (<2 Pa) and disagree with findings from Carpenter (1963) at the level of 6 Pa. Nonetheless, the fidelity of the purely observation-based stationary tidal signal is such that it allows for a rebuttal of the S_2^0 prediction from JRA at the equator and the entire Northern Hemisphere.

7. Conclusions

The present study has documented the creation of a novel collection of mean annual S_1 and S_2 air pressure tide estimates for nearly 6900 land stations and ocean boxes on the basis of ISPDv2 barometric reports for the 1990–2010 period. These data were prefiltered in compliance with accompanying usability flags and subject to a customized quality control of the harmonic analysis at each individual station. The accuracy of the deduced compilation appears to surpass that of any previously published network of similar comprehensiveness, suggesting that both the in situ estimates as well as their multiquadric fits to a global 1° grid can be a reasonable standard with which barometric tidal oscillations in climate models and assimilation systems are validated.

A tentative comparison to S_1 and S_2 climatologies from three current atmospheric reanalyses and one operational analysis testifies to a realistic empirical representation of even the small (~15 Pa) zero-wavenumber components, whose latitudinal structure is not necessarily unambiguous in the numerical models. Much more to the point, the newly proposed S_2 solution—unaffected by gross outliers, subjective smoothing, and a coarsely resolved wavenumber spectrum—indicates migrating semidiurnal peak amplitudes to be in the

range of 123 Pa and thus 10–15 Pa higher than hitherto thought. A persistent overestimation of S_2^2 by 5%–18% in global analysis models is readily apparent and the ramifications of this mismatch for routinely deduced geophysical products (atmospheric loading, pressure forcing of hydrodynamic ocean tidal models) should be examined. In addition, our observational basis will likely foster refined assessments of the tide simulation quality in recent climate models, specifically regarding the impact of finite vertical domains in creating spurious semidiurnal wave reflections and in reducing the amount of stratospheric ozone heating. Migrating tide phases have not been addressed in detail in the above discussions but appear at robust means of 0610 (S_1^1) and 0945 LST (S_2^2) at latitudes below 30°, conforming much better to simulated phases (Covey et al. 2014) than previously suggested in situ solutions (DW).

Our confinement to the mean annual pressure tide components remains a major deficiency to the inferred ground truth dataset and its gridded variant. Respective extensions are, however, envisaged, and we will investigate to what extent the presented harmonic data analysis can be fragmented for different seasons by automated means. Moreover, the spatial coverage of areas holding potentially interesting tidal variability (Andes, central Africa, Southern Hemisphere oceans) is still imperfect and could possibly be improved by loosened restrictions on the local pressure time series or alternative binning strategies. Densifications in these regions will also likely ensue from future versions of the ISPD that are currently underway.

Acknowledgments. We are indebted to Dr. Aiguo Dai for making his datasets freely available via his public website. Author M.S. thanks the Austrian Science Fund (FWF) for financial support within project I1479-N29. Author R.D.R. was supported by the U.S. National Aeronautics and Space Administration through the GRACE and Ocean Surface Topography projects. We greatly appreciate the meteorological data services supplied by the ECMWF and JMA, as well as NASA's GMAO, and we thank Thomas Cram of NCAR for his assistance in downloading the different ISPDv2 subsets. (Support for the ISPD is generally provided by the U.S. Department of Energy, Office of Science Innovative and Novel Computational Impact on Theory and Experiment program, and Office of Biological and Environmental Research, and by the National Oceanic and Atmospheric Administration Climate Program Office.) Comments from David Salstein and Harald Schuh are appreciated as well.

The analysis of stationwise barometer series was performed in the frame of the first author's Ph.D. thesis and is also documented in Schindelegger (2014). Pressure tide estimates at land and marine points (full network, subsetted into three quality classes) as well as the deduced MQI grids can be downloaded at http://ggosatm.hg.tuwien.ac.at/tides.html.

REFERENCES

Bechtold, P., J.-P. Chaboureau, A. Beljaars, A. K. Betts, M. Köhler, M. Miller, and J.-L. Redelsperger, 2004: The simulation of the diurnal cycle of convective precipitation over land in a global model. *Quart. J. Roy. Meteor. Soc.,* **130,** 3119–3137, doi:10.1256/qj.03.103.

Carpenter, T. H., 1963: The distribution of the semidiurnal pressure oscillation on the Antarctic continent. *J. Geophys. Res.,* **68,** 2211–2215, doi:10.1029/JZ068i008p02211.

Chapman, S., and R. Lindzen, 1970: *Atmospheric Tides.* D. Reidel, 200 pp.

Compo, G. P., and Coauthors, 2010: International Surface Pressure Databank (ISPDv2) 1768 to 2010. Research Data Archive at the National Center for Atmospheric Research, Computational and Information Systems Laboratory, Boulder, CO, digital media, doi:10.5065/D6SQ8XDW.

——, and Coauthors, 2011: The Twentieth Century Reanalysis Project. *Quart. J. Roy. Meteor. Soc.,* **137,** 1–28, doi:10.1002/qj.776.

Covey, C., A. Dai, D. Marsh, and R. S. Lindzen, 2011: The surface-pressure signature of atmospheric tides in modern climate models. *J. Atmos. Sci.,* **68,** 495–514, doi:10.1175/2010JAS3560.1.

——, ——, R. S. Lindzen, and D. R. Marsh, 2014: Atmospheric tides in the latest generation of climate models. *J. Atmos. Sci.,* **71,** 1905–1913, doi:10.1175/JAS-D-13-0358.1.

Dai, A., and J. Wang, 1999: Diurnal and semidiurnal tides in global surface pressure fields. *J. Atmos. Sci.,* **56,** 3874–3891, doi:10.1175/1520-0469(1999)056<3874:DASTIG>2.0.CO;2.

——, and K. E. Trenberth, 2004: The diurnal cycle and its depiction in the Community Climate System Model. *J. Climate,* **17,** 930–951, doi:10.1175/1520-0442(2004)017<0930:TDCAID>2.0.CO;2.

Dee, D. P., and Coauthors, 2011: The ERA-Interim reanalysis: Configuration and performance of the data assimilation system. *Quart. J. Roy. Meteor. Soc.,* **137,** 553–597, doi:10.1002/qj.828.

Ebita, A., and Coauthors, 2011: The Japanese 55-year Reanalysis "JRA-55": An interim report. *SOLA,* **7,** 149–152, doi:10.2151/sola.2011-038.

Forbes, J. M., and H. B. Garrett, 1979: Theoretical studies of atmospheric tides. *Rev. Geophys.,* **17,** 1951–1984, doi:10.1029/RG017i008p01951.

Hagan, M. E., and J. M. Forbes, 2002: Migrating and nonmigrating diurnal tides in the middle and upper atmosphere excited by tropospheric latent heat release. *J. Geophys. Res.,* **107,** 4754, doi:10.1029/2001JD001236.

——, and ——, 2003: Migrating and nonmigrating semidiurnal tides in the middle and upper atmosphere excited by tropospheric latent heat release. *J. Geophys. Res.,* **108,** 1062, doi:10.1029/2002JA009466.

——, ——, and A. Richmond, 2003: Atmospheric tides. *Encyclopedia of Atmospheric Sciences,* J. Holton, J. Pyle, and J. Curry, Eds., 1st ed. Academic Press, 159–165.

Hamilton, K., 1980a: Observations of the solar diurnal and semidiurnal surface pressure oscillations in Canada. *Atmos.–Ocean,* **18,** 89–97, doi:10.1080/07055900.1980.9649080.

——, 1980b: The geographical distribution of the solar semidiurnal surface pressure oscillation. *J. Geophys. Res.,* **85,** 1945–1949, doi:10.1029/JC085iC04p01945.

——, S. C. Ryan, and W. Ohfuchi, 2008: Topographic effects on the solar semidiurnal surface tide simulated in a very fine resolution general circulation model. *J. Geophys. Res.,* **113,** D17114, doi:10.1029/2008JD010115.

Haurwitz, B., 1956: The geographical distribution of the solar semidiurnal pressure oscillation. *N. Y. Univ. Coll. Eng. Meteor. Pap.,* **2** (5), 1–36.

——, and A. D. Cowley, 1973: The diurnal and semidiurnal barometric oscillations, global distribution and annual variation. *Pure Appl. Geophys.,* **102,** 193–222, doi:10.1007/BF00876607.

Hsu, H. H., and B. J. Hoskins, 1989: Tidal fluctuations as seen in ECMWF data. *Quart. J. Roy. Meteor. Soc.,* **115,** 247–264, doi:10.1002/qj.49711548603.

Jin, S., O. F. Luo, and S. Gleason, 2009: Characterization of diurnal cycles in ZTD from a decade of global GPS observations. *J. Geod.,* **83,** 537–545, doi:10.1007/s00190-008-0264-3.

Kong, C.-W., 1995: Diurnal pressure variations over continental Australia. *Aust. Meteor. Mag.,* **44,** 165–175.

Li, Y., R. B. Smith, and V. Grubišić, 2009: Using surface pressure variations to categorize diurnal valley circulations: Experiments in Owens Valley. *Mon. Wea. Rev.,* **137,** 1753–1769, doi:10.1175/2008MWR2495.1.

Mass, C. F., W. J. Steenburgh, and D. M. Schultz, 1991: Diurnal surface-pressure variations over the continental United States and the influence of sea level reduction. *Mon. Wea. Rev.,* **119,** 2814–2830, doi:10.1175/1520-0493(1991)119<2814:DSPVOT>2.0.CO;2.

Nuss, W. A., and D. W. Titley, 1994: Use of multiquadric interpolation for meteorological objective analysis. *Mon. Wea. Rev.,* **122,** 1611–1631, doi:10.1175/1520-0493(1994)122<1611:UOMIFM>2.0.CO;2.

Persson, A., 2011: User guide to ECMWF forecast products. ECMWF Publ., 119 pp. [Available online at http://old.ecmwf.int/newsevents/meetings/forecast_products_user/Guide_2011-print.pdf.].

Petrov, L., and J.-P. Boy, 2004: Study of the atmospheric pressure loading signal in very long baseline interferometry observations. *J. Geophys. Res.,* **109,** B03405, doi:10.1029/2003JB002500.

Ray, R. D., 1998: Diurnal oscillations in atmospheric pressure at twenty-five small oceanic islands. *Geophys. Res. Lett.,* **25,** 3851–3854, doi:10.1029/1998GL900039.

——, 2001: Comparisons of global analyses and station observations of the S_2 barometric tide. *J. Atmos. Sol.-Terr. Phys.,* **63,** 1085–1097, doi:10.1016/S1364-6826(01)00018-9.

——, and R. M. Ponte, 2003: Barometric tides from ECMWF operational analyses. *Ann. Geophys.,* **21,** 1897–1910, doi:10.5194/angeo-21-1897-2003.

——, and S. Poulose, 2005: Terdiurnal surface-pressure oscillations over the continental United States. *Mon. Wea. Rev.,* **133,** 2526–2534, doi:10.1175/MWR2988.1.

Rienecker, M. M., and Coauthors, 2011: MERRA: NASA's Modern-Era Retrospective Analysis for Research and Applications. *J. Climate,* **24,** 3624–3648, doi:10.1175/JCLI-D-11-00015.1.

Sato, T., T. Yoshikane, M. Satoh, H. Miura, and H. Fujinami, 2008: Resolution dependency of the diurnal cycle of convective clouds over the Tibetan plateau in a mesoscale model. *J. Meteor. Soc. Japan,* **86A,** 17–31, doi:10.2151/jmsj.86A.17.

Schindelegger, M., 2014: Atmosphere-induced short period variations of Earth rotation. Geowissenschaftliche Mitteilungen Heft 96, Vienna University of Technology, 152 pp. [Available online at http://publik.tuwien.ac.at/files/PubDat_228266.pdf.]

Simpson, G. C., 1918: The twelve-hourly barometer oscillation. *Quart. J. Roy. Meteor. Soc.,* **44,** 1–19, doi:10.1002/qj.49704418501.

Stone, M., 1974: Cross-validatory choice and assessment of statistical predictions. *J. Roy. Stat. Soc.,* **36B** (2), 111–147.

Tsuda, T., and S. Kato, 1989: Diurnal nonmigrating tides excited by a differential heating due to land-sea distribution. *J. Meteor. Soc. Japan,* **67,** 43–55.

Ueyama, R., and C. Deser, 2008: A climatology of diurnal and semidiurnal surface wind variations over the tropical Pacific Ocean based on the tropical atmosphere ocean moored buoy array. *J. Climate,* **21,** 593–607, doi:10.1175/JCLI1666.1.

van den Dool, H. M., S. Saha, J. Schemm, and J. Huang, 1997: A temporal interpolation method to obtain hourly atmospheric surface pressure tides in Reanalysis 1979–1995. *J. Geophys. Res.,* **102,** 22 013–22 024, doi:10.1029/97JD01571.

Watson, D., 1999: The natural neighbor series manuals and source codes. *Comput. Geosci.,* **25,** 463–466, doi:10.1016/S0098-3004(98)00150-2.

Yseboodt, M., O. de Viron, T. M. Chin, and V. Dehant, 2002: Atmospheric excitation of the Earth's nutation: Comparison of different atmospheric models. *J. Geophys. Res.,* **107,** 2036, doi:10.1029/2000JB000042.

Zhang, X., J. M. Forbes, M. E. Hagan, J. M. Russell III, S. E. Palo, C. J. Mertens, and M. G. Mlynczak, 2006: Monthly tidal temperatures 20–120 km from TIMED/SABER. *J. Geophys. Res.,* **111,** A10S08, doi:10.1029/2005JA011504.

Zwiers, F., and K. Hamilton, 1986: Simulation of solar tides in the Canadian Climate Centre general circulation model. *J. Geophys. Res.,* **91,** 11 877–11 896, doi:10.1029/JD091iD11p11877.